Available online at www.sciencedirect.com
ScienceDirect
International Journal of Heat and Fluid Flow 29 (2008) 1071–1088
International Journal of HEAT AND FLUID FLOW
www.elsevier.com/locate/ijhff

Large eddy simulation of flow around wavy cylinders at a subcritical Reynolds number

K. Lam *, Y.F. Lin

Department of Mechanical Engineering, The Hong Kong Polytechnic University, Hong Kong

Received 24 January 2007; received in revised form 17 December 2007; accepted 14 January 2008
Available online 10 March 2008

Abstract

The cross-flow around wavy cylinders of wavelength ratios λ/D_m from 1.136 to 3.333 are investigated at $Re = 3000$ using large eddy simulation (LES). The mean flow field and the near wake flow structures are presented and compared with those of a circular cylinder at the same Reynolds number. The mean pressure distributions are also calculated. The results show that the mean drag coefficients of the wavy cylinders are less than those of a corresponding circular cylinder due to a longer wake vortex formation length generated by the wavy cylinders. For a subcritical Reynolds number of 3000, a maximum drag coefficient reduction of up to 18% compared with a circular cylinder is obtained corresponding to an optimal wavelength ratio of λ/D_m around 1.9 and an amplitude ratio a/D_m of 0.152. The fluctuating lift coefficients of the wavy cylinders are also greatly reduced or even suppressed. These kinds of wavy surfaces lead to the formation of three-dimensional free shear layers which are more stable than purely two-dimensional free shear layers. Such free shear layers will only roll up into mature vortices at further downstream positions. This significantly modified the near wake structures and the pressure distribution around the cylinder. It was found that the wave amplitude to wavelength ratio a/λ plays an essential role in determining the 3D vortex structure behind the wavy cylinders which has a significant effect on the reduction of the fluctuating lift and suppression of flow-induced vibration.

Keywords: Wavy cylinders; Drag reduction; Turbulent flow; Large eddy simulation

1. Introduction

Flow around cylindrical bodies gives rise to many complex flow phenomena at subcritical Reynolds numbers. The alternate vortex shedding from these bluff bodies will produce very complicated flow effects such as causing vibration known as vortex induced vibration (VIV). Flow over circular cylinders has been extensively investigated by many researchers. How to control vortex shedding and hence reduce the flow-induced vibration becomes a challenging problem in the fluid dynamics arena. One of the methods to control vortex shedding is by adding some objects on or near the cylinders. Another method is by modifying the geometry of the cylindrical structures. Three-dimensional free shear layers developed from these kinds of cylinders will give rise to complex vortex structures which in turn leads to the reduction of lift and drag forces and hence the suppression of vibration.

Based on the latter ideas of modifying the geometry of the bluff bodies, Tomabzis and Bearman (1997) and Bearman and Owen (1998a,b) applied a spanwise wave deformation to the trailing and leading face of a half-ellipse shape body and a square cylinder, respectively. By modifying the leading face of a square cylinder, the maximum drag force reduction over 30% at the Reynolds number about 40,000 was obtained. Later, Owen et al. (2000) studied flow past a sinuous cylinder by flow visualization method. The Kármán vortex shedding was well suppressed and a periodic variation in the wake width across the spanwise direction was observed. Darekar and Sherwin (2001a,b) numerically investigated the flow past a square

* Corresponding author. Tel.: +852 2766 6649; fax: +852 2365 4703.
E-mail address: mmklam@polyu.edu.hk (K. Lam).

0142-727X/$ - see front matter © 2008 Elsevier Inc. All rights reserved.
doi:10.1016/j.ijheatfluidflow.2008.01.006

cylinder with a wavy stagnation face at low Reynolds numbers. The steady nature of the near wake is associated with a reduction in total drag of about 16% at a Reynolds number of 100 compared with the straight, non-wavy square cylinder. Moreover, at higher Reynolds numbers, the drag force reduction increases substantially.

Similar to the works mentioned above, another type of cylinder whose diameter varies sinusoidally along its spanwise direction, called a wavy cylinder, was introduced and studied by the present investigators (see Fig. 1). It was hoped that such a type of cylinder could lead to better control of the vortex shedding and hence the suppression of flow-induced vibration of a cylindrical structure. Previously, experimental investigations on the surface-pressure distributions of wavy cylinders with different spanwise wavelengths have been carried out by Ahmed and Bays-Muchmore (1992). They found that the separated flow structures near the geometric nodes are distinctly asymmetric for a large fraction of time and the sectional drag coefficients at the geometric nodes are greater than these at the geometric saddle. Ahmed et al. (1993) further investigated experimentally the turbulent wake behind a wavy cylinder. He described the topology of the boundary layer separation lines and the subsequent 3D development of the turbulent structure of the wake. As a result, they found that the formation of trailing streamwise vortices behind the nodal points of separation gave rise to a locally narrower wake, a rapid wake-velocity recovery and a suppression of the turbulence development within the separated boundary layer. But the drag reduction and suppression of vibration were not discussed. Keser et al. (2001) used a 3D discrete vortex method to simulate the separated flow around wavy cylinders. Lam et al. (2004a) started to focus attention on effects of different wavy cylinders on drag and lift reduction and the related flow-induced vibration experimentally in the range of subcritical Reynolds numbers from 20,000 to 50,000. They found that drag reduction of up to 20% could be achieved by changing the geometric wavelength and wave amplitude of the cylinder. It was also found that the root-mean-square fluctuating lift coefficients of the wavy cylinders are much lower than those of the circular cylinders. Furthermore, Lam et al. (2004b) investigated the near wake of a wavy cylinder using the Laser Doppler Velocimetry (LDV) measurement. Compared to a circular cylinder, the wavy geometry played an important role on vortex formation length, drag reduction and vortex shedding suppression. The vortex formation length of the wavy cylinder is longer than that of the circular cylinder. In the wake of the wavy cylinder, the rib structures were detected near the saddle planes by using the laser-induced fluorescence (LIF) method at a Reynolds number of 600. This gives rise to a longer formation length which has a strong link with the effects of the drag force reduction. At the nodal and saddle plane, the streamwise velocity distributions are very different compared with a circular cylinder. Also the Reynolds stress is suppressed. On the other hand, Nguyen and Jee (2004) investigated the near wake behind a wavy cylinder by using hot-wire anemometer and flow visualization. Drag reduction up to 22% at a Reynolds number of 10,000 was obtained. They also showed that the longer vortex formation region of the wavy cylinder seems to be related to drag reduction. At the same Reynolds numbers, the vortex formation length is longer and the turbulence intensity is smaller than that of a circular cylinder. Recently, Zhang et al. (2005) investigated the three-dimensional near wake structures behind a wavy cylinder by using particle image velocimetry (PIV) technique at a Reynolds number of 3000. Along the span of a wavy cylinder, well-organized streamwise vortices with alternating positive and negative vortices were observed. They suppress the formation of the large-scale spanwise vortices and decrease the overall turbulent kinetic energy in the near wake of the wavy cylinder. In efforts of numerical simulation, Lam and Lin (2006) also captured the detailed three-dimensional vortex structures of three wavy cylinders by using the large eddy simulations (LES).

All the investigations mentioned above have only been studied over a small region of the wavelengths ($1.0 < \lambda/D_m < 2.27$) along the spanwise direction. The optimal value of wavelength which can control the vortex formation is still not known. Furthermore, the amplitude of the wavy cylinder also plays an important role in the control of the vortex structure from the wavy cylinders. Moreover, the three-dimensional vortex structures can not be illustrated

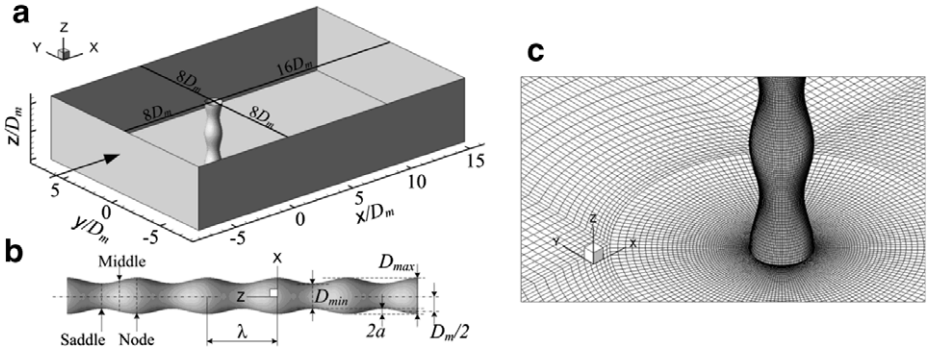

Fig. 1. Computational models: (a) schematic of the computational domain, (b) geometry of a wavy cylinder and (c) grid distributions around the wavy cylinder.

clearly using experimental methods especially at subcritical Reynolds numbers. It is anticipated that numerical simulations can well capture the instantaneous three-dimensional vortex structures and other valuable data, such as drag, lift, pressure, velocity and Reynolds stress, etc. For turbulent flow, large eddy simulation method is becoming a very popular CFD method. It is capable of simulating the complex turbulent flows behind the cylinders. In the present study, the three-dimensional wavy cylinders with different wave geometrics are studied using the LES method. The relationship between spanwise wavelength, wave amplitude, and force coefficients are investigated. The optimal wavelength is sought. The three-dimensional vortex structures are replicated; the pressure, velocity, separation angle, and the Strouhal numbers are also calculated.

2. Computational models

2.1. Governing equations and the subgrid model

By using the three-dimensional LES turbulence model, the large scale eddies are solved directly by the filtered Navier–Stokes equations, and the small eddies are modeled using a subgrid scale (SGS) model. The large-scale turbulence motions are strongly dependent on the flow geometry and boundary conditions, and they can be predicted by the resolved flow in the LES method. On the other hand, the subgrid scale model represents the small-scale eddy motion which is more universal in character than the large scale eddy. The filtering operation proceeds according to

$$\bar{\phi} = \frac{1}{\Delta}\int_{\Delta}\phi(x')\mathrm{d}x', \quad x' \in \Delta, \tag{1}$$

$$G(x,x') = \begin{cases} 1/\Delta, & x' \in \Delta \\ 0, & \text{otherwise} \end{cases} \tag{2}$$

where Δ is the volume of a computational cell, and $G(x,x')$ is a filter function. Applying the filtering operation, the incompressible Navier–Stokes equations for the evolution of the large-scale motions are obtained. The governing equations employed for LES are

$$\frac{\partial \bar{u}_i}{\partial x_i} = 0, \tag{3}$$

$$\frac{\partial \bar{u}_i}{\partial t} + \frac{\partial \bar{u}_i\bar{u}_j}{\partial x_j} = -\frac{1}{\rho}\frac{\partial \bar{p}}{\partial x_i} + \nu\frac{\partial^2 \bar{u}_i}{\partial x_j \partial x_j} - \frac{\partial \tau_{ij}}{\partial x_j}, \quad (i = 1,2,3) \tag{4}$$

where $\bar{u}_i$ are the filtered velocity components along the Cartesian coordinates x_i, $\bar{p}$ is the pressure, ρ is the fluid density and ν is the kinematic viscosity of the fluid. The influence of the small scales on the large (resolved) scales takes place through the subgrid scale stress defined by

$$\tau_{ij} = \overline{u_i u_j} - \bar{u}_i\bar{u}_j, \tag{5}$$

resulting from the filtering operation, which are unknown and must be modeled with a subgrid model. The majority of subgrid scale models are based on the eddy viscosity models of the following form:

$$\tau_{ij} - \frac{1}{3}\tau_{kk}\delta_{ij} = -2\nu_t\overline{S}_{ij}, \tag{6}$$

where the trace of the subgrid scale stresses τ_{kk} is incorporated in the pressure resulting in a modified pressure term, ν_t is the subgrid-scale kinematic viscosity, and $\overline{S}_{ij}$ is the strain rate tensor for the resolved scale defined by

$$\overline{S}_{ij} = \frac{1}{2}\left(\frac{\partial \bar{u}_i}{\partial x_j} + \frac{\partial \bar{u}_j}{\partial x_i}\right) \tag{7}$$

The most basic of subgrid scale models is proposed by Smagorinsky (1963) and further developed by Lilly (1966). In the Smagorinsky–Lilly model, the subgrid kinematic viscosity ν_t is modeled by

$$\nu_t = l_s^2|\overline{S}_{ij}| \tag{8}$$

where l_s is the mixing length for the subgrid scales, and $|\overline{S}_{ij}| \equiv \sqrt{2\overline{S}_{ij}\overline{S}_{ij}}$. l_s can be computed using

$$l_s = \min(ky, C_s\Delta^{1/3}) \tag{9}$$

where k is the von Kármán constant ($k = 0.42$) and y is the distance to the nearest wall. C_s is the Smagorinsky constant, and Δ is the volume of the computational cell.

Lilly (1966) derived a value of 0.23 for C_s from homogeneous isotropic turbulence in the inertial subrange. However, this kind of large C_s value was found to cause excessive damping of the large-scale fluctuations in the presence of mean shear or in transitional flows, and small values ($C_s < 0.1$) may cause convergence problems. For many investigators, the Smagorinsky constant ($C_s = 0.1$–0.14) has been found to yield good results for a wide range of flows. All computations in the present work were carried out with a Smagorinsky constant of $C_s = 0.1$, which is found to be a suitable value for the applications of the Smagorinsky model to turbulent wake simulation.

2.2. Numerical method

In the present simulation, the finite-volume method (FVM) applied on unstructured grids is employed to calculate the 3D unsteady incompressible Navier–Stokes equation. A second-order central differencing scheme is used for momentum discretization while a second-order implicit scheme is employed to advance the equations in time. The well-known pressure implicit method with splitting of operators (PISO) algorithm is used to deal with the pressure–velocity coupling between the momentum and the continuity equations.

2.3. Computational domain and boundary conditions

The computational domain used for the simulations is shown in Fig. 1a. The dimension of it is set at $L_x \times L_y \times L_z$ in the x, y, z directions of a fixed Cartesian coordinate system (x,y,z). A wavy cylinder model is set inside it. The origin of the coordinate system is located at the end of the wavy cylinder. The x-axis is aligned with the inlet flow

direction (streamwise direction), the z-axis is parallel to the cylinder axis (spanwise direction) and the y-axis is perpendicular to both the x and z axes (crosswise direction). As shown in Fig. 1b, the geometry of the wavy cylinders is described by the equation, $D_z = D_m + 2a\cos(2\pi z/\lambda)$. Here, D_z denotes the local diameter of the wavy cylinder and the mean diameter is defined with $D_m = (D_{min} + D_{max})/2$. D_{min} is the minimum diameter of cylinder along the spanwise direction, while D_{max} is the maximum diameter of the wavy cylinder. The amplitude of the curve surface is denoted by 'a', and 'λ' is the wavelength along the spanwise direction. The axial locations with maximum local diameter are referred to as "nodes", while the axial locations of the minimum diameter are called "saddles". The "middle" is also defined at mid-point between the node and the saddle.

In the present study, the different wavy cylinders are investigated systematically. As shown in Table 1, there are eleven wavy cylinder models with different combinations of wave amplitude a/D_m and spanwise wavelength λ/D_m in the present simulations. By grouping the value of a/D_m, equal to 0.091 and 0.152, these models are classified into two groups which are named "WY-A" and "WY-B", respectively. In group "WY-A" ($a/D_m = 0.091$), there are five wavy cylinder models (WY-A1, WY-A2, WY-A3, WY-A4, WY-A5) each with different value of $\lambda/D_m =$ 1.136, 1.515, 1.894, 2.273 and 2.818, respectively, while there are six models (WY-B1, WY-B2, WY-B3, WY-B4, WY-B5, WY-B6) in group "WY-B" ($a/D_m = 0.152$) and each with different value of $\lambda/D_m =$ 1.136, 1.515, 1.894, 2.273, 2.818 and 3.333, respectively. All the wavy cylinder cases are simulated and compared with corresponding circular cylinders under the same simulation conditions.

In solving the governing equations, the different physical quantities are changed to a nondimensional form, i.e., all the variables are normalized. All geometrical lengths are scaled with D_m. In the present simulations, taking the examples of the computational domain adopted by previously investigations for flow pass bluff bodies at subcritical Reynolds numbers using the LES method, for example $L_x \times L_y \times L_z = 23.2 \times 15.7 \times 4$ by Sohankar et al. (2000), and $L_x \times L_y \times L_z = 18.8 \times 10 \times \pi$ by Liang and Papadakis (2007), in the streamwise and crosswise directions (see Fig. 1a), the computational boundaries L_x and L_y are set at $24D_m$ and $16D_m$, respectively. The upstream boundary is set at $8D_m$ away from the centerline of wavy cylinder. The downstream boundary is $16D_m$ away from the wavy cylinder. The experimental studies of Williamson et al. (1995) and Williamson (1996) showed that the wavelength of the streamwise vortex structures in the near wake of a circular cylinder scales is given by $\lambda_z/D_m \approx 25Re^{-1/2}$. Here, λ_z is the spanwise wavelength of the vortices and the Reynolds number based on the mean diameter of wavy cylinder is fixed at $Re = D_m U_\infty/\nu = 3000$ for all the cases studied. So the estimated near wake wavelength of streamwise vortices for the circular cylinder is around$0.5D_m$. Further downstream, the large scale structures for streamwise vortices with wavelengths $\lambda_z/D_m \approx 1$ have been reported (Williamson (1996)). Considering the resolution of the large scale eddies, we use L_z at the range of $2.82D_m$ to $4.55D_m$ in the spanwise direction which will be sufficient for the present simulations for the circular cylinder (see Table 2). As mentioned by Lam et al. (2004b) and Zhang et al. (2005), the periodic repeated vortex structures were observed to be consistent with the periodic repetition of the wavy cylinder spanwise wavelength λ. In the present simulation, the spanwise domain L_z of the wavy cylinders are set equal to the same range as that of the circular cylinders (2.82–$4.55D_m$) in the spanwise direction. In order to save computation time, spanwise domain length to wavelength ratios (L_z/λ) of 4, 3, 2 and 1 are employed as λ/D_m increases from 1.136 to 3.333 (see Table 1).

Table 1
Computational models parameters for different wavy cylinders

Wavy models	λ/D_m	a/D_m	$L_x \times L_y \times L_z$ (D_m)	Grid
WY-A1	1.136	0.091	$24 \times 16 \times 4.55$	$16{,}000 \times 80$
WY-A2	1.515	0.091	$24 \times 16 \times 4.55$	$16{,}000 \times 80$
WY-A3	1.894	0.091	$24 \times 16 \times 3.79$	$16{,}000 \times 64$
WY-A4	2.273	0.091	$24 \times 16 \times 4.55$	$16{,}000 \times 80$
WY-A5	2.818	0.091	$24 \times 16 \times 2.82$	$16{,}000 \times 48$
WY-B1	1.136	0.152	$24 \times 16 \times 4.55$	$16{,}000 \times 80$
WY-B2	1.515	0.152	$24 \times 16 \times 4.55$	$16{,}000 \times 80$
WY-B3	1.894	0.152	$24 \times 16 \times 3.79$	$16{,}000 \times 64$
WY-B4	2.273	0.152	$24 \times 16 \times 4.55$	$16{,}000 \times 80$
WY-B5	2.818	0.152	$24 \times 16 \times 2.82$	$16{,}000 \times 48$
WY-B6	3.333	0.152	$24 \times 16 \times 3.33$	$16{,}000 \times 64$

The computational domain is divided into a number of unstructured hexahedral grids. Fig. 1c shows that the grid is nonuniform on the x–y plane but uniform along the z-direction. The grid is clustered near the cylinder and the spacing is increased in a proper ratio away from the cylinder. The distance from the cylinder surface to the nearest grid points are fixed at y^+ close to 1. At the inlet boundary, a uniform velocity profile ($u = 1$, $v = w = 0$) is imposed, while the convective boundary condition ($\partial u_i/\partial t + U_c(\partial u_i/\partial x) = 0$) is used at the outlet boundary (Breuer, 1998; Sohankar et al., 2000), where U_c is the convection velocity equal to the mean velocity at the inlet. A periodic boundary condition is employed at the boundaries in the spanwise direction and a no-slip boundary condition ($u = v = w = 0$) is prescribed at the surface of the wavy cylinders. The lateral surfaces are treated as slip surfaces using symmetry conditions ($\partial u/\partial y = \partial w/\partial y = v = 0$).

2.4. Grid independence and the validation of numerical models

The accuracy of the computational results using LES is highly dependent on the mesh size and cell numbers. The grid test calculations must be carried out first. Table 2 shows that seven circular cylinder models are constructed for LES simulation and the results are compared with experimental and other numerical results of circular cylin-

Table 2
Grid independence test for a circular cylinder at $Re = 3000$

Circular cylinder	Re		$\bar{C}_D$	C'_L	St
Norberg (1987) (experimental)	3000		0.98–1.03	N/A	0.210–0.213
Norberg (2003) (summarized)	3000 (3900)		N/A	0.05, 0.07 (0.07, 0.3)	0.210 (0.208)
Lu et al. (1997) (experimental)	3000		1.02	N/A	N/A
Lu et al. (1997) (LES) 3D	3000		1.07	0.48	N/A
Present cases	$L_x \times L_y \times L_z$ (D_m)	Grid	$\bar{C}_D$	C'_L	St
Coarse-grid 1 (LES) 3D	$24 \times 16 \times 4.55$	$10{,}900 \times 64$	1.21	0.385	0.207
Coarse-grid 2 (LES) 3D	$24 \times 16 \times 4.55$	$13{,}620 \times 64$	1.11	0.221	0.209
Fine-grid 1 (LES) 3D	$24 \times 16 \times 2.82$	$16{,}000 \times 48$	1.08	0.188	0.210
Fine-grid 2 (LES) 3D	$24 \times 16 \times 3.33$	$16{,}000 \times 64$	1.10	0.195	0.211
Fine-grid 3 (LES) 3D	$24 \times 16 \times 4.55$	$16{,}000 \times 64$	1.09	0.174	0.210
Fine-grid 4 (LES) 3D	$24 \times 16 \times 4.55$	$16{,}000 \times 80$	1.09	0.177	0.210
Fine-grid 5 (LES) 3D	$24 \times 16 \times 4.55$	$21{,}200 \times 80$	1.08	0.183	0.211

ders at $Re = 3000$. The grid independence inspection for the three-dimensional flow simulations was carried out prior to extensive numerical simulation. For these seven cases, the mesh numbers set to 120, 144, 160 and 200 around the cylinder circumference corresponding to the cells in x–y plane are from 10,900, 13,620, 16,000 and 21,200, respectively. Uniform layer from 48 to 80 are used along the z-direction. The mean drag coefficients of the circular cylinders ($\bar{C}_D$) in our simulations (Fine-grid 1–5) are in good agreement with the 3D LES results taken from Lu et al. (1997), and slightly larger than those of the experimental data (Norberg, 1987; Lu et al., 1997). The fluctuating lift coefficients (C'_L) of the present circular cylinder cases are around the value of 0.18 at $Re = 3000$ which are slightly larger than the experimental results summarized by Norberg (2003) ($C'_L = 0.05$ or 0.07, $Re = 3000$, and $C'_L = 0.07$, $Re = 3900$). However, the values are smaller than those 3D simulation results $C'_L = 0.48$ at $Re = 3000$ by Lu et al. (1997) and $C'_L = 0.3$ at $Re = 3900$ summarized by Norberg (2003). Due to the great spread in the value of C'_L obtained by different investigators, the present result of fluctuating lift coefficient C'_L is also within such range and is considered to be acceptable. The Strouhal numbers ($St = f_s D_m / U_\infty$) of the present results also agree with the experimental measurements. Here, f_s is the vortex shedding frequency. With different grid numbers, grid independence tests are satisfied considering the variation of the values of $\bar{C}_D$, C'_L and St except for the models of Coarse-grid 1 and 2. For the wavy cylinders, the grid independence tests (Table 3) are also performed. A typical wavy cylinder model WY-A4 ($a/D_m = 0.091$, $\lambda/D_m = 2.273$) with four different grid numbers (coarse-grid models 1, 2 and Fine-grid models 4 and 5) is calculated apart from the calculations of the circular cylinder cases with the same grid number. As shown in Table 3, there are only very little difference on the values of $\bar{C}_D$, C'_L and St for the wavy cylinder models of Fine-grid 4 and 5 compared with the models of the coarse-grid 1 and 2. This is similar to the conclusion for circular cylinder tests discussed above. Other tests for the effect of grid refinement will be discussed in Section 3.1 (see Figs. 2–4).

To ensure better results and capture detailed vortex structures, the finer grid number of 16,000 in the x–y plane is adopted for all the simulations of the present wavy and circular cylinder cases. On the other hand, the uniform layers from 48 to 80 are used along the cylinder spanwise direction. A nondimensional time step $\Delta t U_\infty / D_m = 0.02$ was chosen for the simulation, yielding the maximum CFL number close to 2 and ensured sufficiently small CFL numbers less than 1 for most part of the computational domain. It was dictated by the numerical stability of the computations. A smaller time step $\Delta t U_\infty / D_m = 0.005$ was also tested for comparison, and the differences between the two time step cases were found to be very small (see Table 3, the cases of Fine-grid 4 (i) and (ii)). Also, as mentioned above, the spanwise lengths L_z of the wavy cylinders in the computational domain are 1–4 wavelengths. For the wavy cylinder models with only one wavelength

Table 3
Grid independence test for a wavy cylinder (WY-A4) and the periodic boundary condition validation test by a wavy cylinder (WY-B6) at $Re = 3000$

Wavy cylinder	Model	$L_x \times L_y \times L_z$ (D_m)	Grid	$\Delta t U_\infty / D_m$	$\bar{C}_D$	C'_L	St
Coarse-grid 1 (LES) 3D	WY-A4	$24 \times 16 \times 4.55$	$10{,}900 \times 64$	0.02	1.09	0.178	0.206
Coarse-grid 2 (LES) 3D	WY-A4	$24 \times 16 \times 4.55$	$13{,}620 \times 64$	0.02	1.00	0.052	0.206
Fine-grid 4 (LES) 3D (i)	WY-A4	$24 \times 16 \times 4.55$	$16{,}000 \times 80$	0.02	0.99	0.039	0.207
Fine-grid 4 (LES) 3D (ii)	WY-A4	$24 \times 16 \times 4.55$	$16{,}000 \times 80$	0.005	0.99	0.044	0.209
Fine-grid 5 (LES) 3D	WY-A4	$24 \times 16 \times 4.55$	$21{,}200 \times 80$	0.02	0.99	0.043	0.208
Fine-grid 2 (LES) 3D (i)	WY-B6	$24 \times 16 \times 3.33$	$16{,}000 \times 64$	0.02	1.01	0.061	0.210
Fine-grid 2 (LES) 3D (ii)	WY-B6	$24 \times 16 \times 6.66$	$16{,}000 \times 128$	0.02	1.01	0.063	0.210

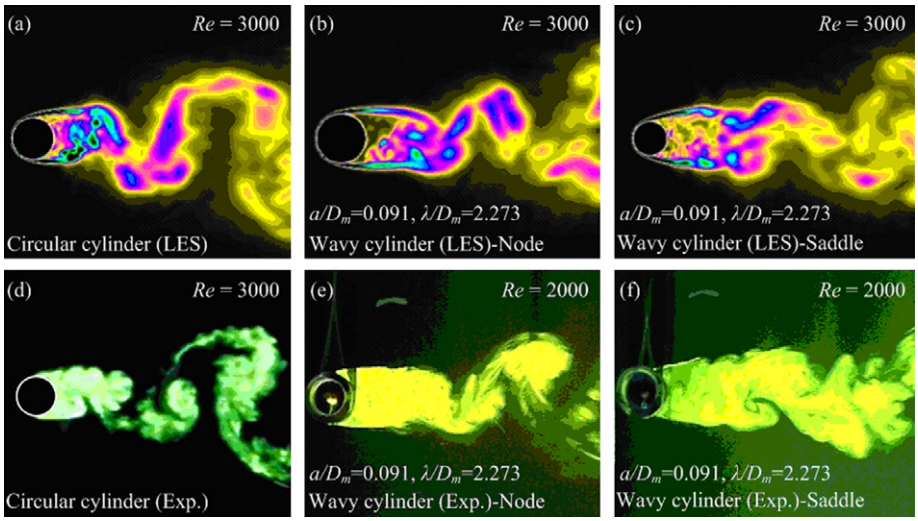

Fig. 2. Vortex structures of a circular cylinder and a wavy cylinder (WY-A4) by LES method (upper) compared with experimental results (lower). (a)–(c) present LES method at $Re = 3000$; (d) LIF result at $Re = 3000$ taken from Dalton and Xu (2001); (e) and (f) LIF results at $Re = 2000$ taken from Lam et al. (2004).

domain in the spanwise direction, the validation of the periodic boundary condition are also carried out by choosing a typical wavy cylinder model WY-B6 which has the largest value of spanwise wavelength $\lambda/D_m = 3.333$ in the present simulations and with $a/D_m = 0.152$. As shown in Table 3, the values of $\bar{C}_D$, C'_L and St are basically the same by using one or two wavelength domain length in the spanwise direction. Therefore, it can be seen that even one wavelength of spanwise domain length can be sufficient for the present simulations. Moreover, other tests of the validation of the periodic boundary condition on the vortex structures and force time histories will be discussed later (see Figs. 14 and 15). For all of the present simulations, at least 150 dimensionless time units (tU_∞/D_m), which corresponded to about 30 vortex-shedding cycles, were taken so as to obtain more reliable statistical information. The overall drag coefficient is defined by $C_D = C_{Dp} + C_{Df} = 2F_D/\rho U_\infty^2 D_m L_z$.Also, the overall lift coefficient is $C_L = C_{Lp} + C_{Lf} = 2F_L/\rho U_\infty^2 D_m L_z$. The total drag force and total lift force are given by F_D and F_L. The pressure drag and pressure lift coefficients are C_{Dp} and C_{Lp}, respectively. Moreover, C_{Df} and C_{Lf} are the skin friction drag and lift forces, respectively which normally contribute a very small percentage of the total force for bluff bodies at high Re. The total drag (and lift) is the sum of friction and pressure drag (and lift) calculations.

3. Results and discussion

3.1. The flow patterns and velocity distributions

Firstly, a wavy cylinder model WY-A4 (Fine-grid 4), with the same combination of amplitude and wavelength ratio of $a/D_m = 0.091$ and $\lambda/D_m = 2.273$ investigated experimentally by Lam et al. (2004b), is investigated at $Re = 3000$. Moreover, a circular cylinder model (Fine-grid 4) is also simulated. The vortex structures of these two different cylinders obtained by an LES model are compared with the laser-induced fluorescence (LIF) results as shown in Fig. 2. It can be clearly seen that, in the present simulation, the near wake formation of a circular cylinder is in good qualitative agreement with the experimental vortex structures at $Re = 3000$ by Dalton and Xu (2001). The wakes of the wavy cylinder at the nodal and saddle plane are also similar to the LIF results by Lam et al. (2004b) at $Re = 2000$.

Fig. 3 shows the comparison of the LES results of the mean streamwise velocity U/U_∞ and fluctuating streamwise velocity u'/U_∞ distributions of the wavy (WY-A4) and circular cylinders with the experimental measurements by a Laser Doppler Anemometry (LDA) method (refer to the wavy and circular cylinder cases with different grid numbers indicated in Tables 2 and 3). For the Coarse-grid models 1 and 2, the LES results of U/U_∞ and u'/U_∞ show a larger discrepancy with that of the LDA results (Norberg, 1998; Lam et al., 2004b and present LDA measurements), especially for the curves with the Coarse-grid model 1. However, only very little discrepancy can be observed between the LES results and experimental results when adopting the Fine-grid model 4 and Fine-grid model 5 grid sizes for both the circular and wavy cylinders. As shown in Fig. 3, for the circular cylinder, the LES results of the distributions of U/U_∞ and u'/U_∞ agree very well with that of the experimental results. This is also the same for the wavy cylinder (WY-A4) at nodal planes. However, in saddle planes at the position of $x/D_m = 3$, an obvious discrepancy of the values of U/U_∞ can be observed from the present LES results and the LDA measurements by Lam et al. (2004b). Considering the discussions by Lam et al. (2004b), the end point of the reverse flow position (the velocity recovery point) in the wake centerline behind the wavy cylinder (WY-A4) at $Re = 3000$ is at around the posi-

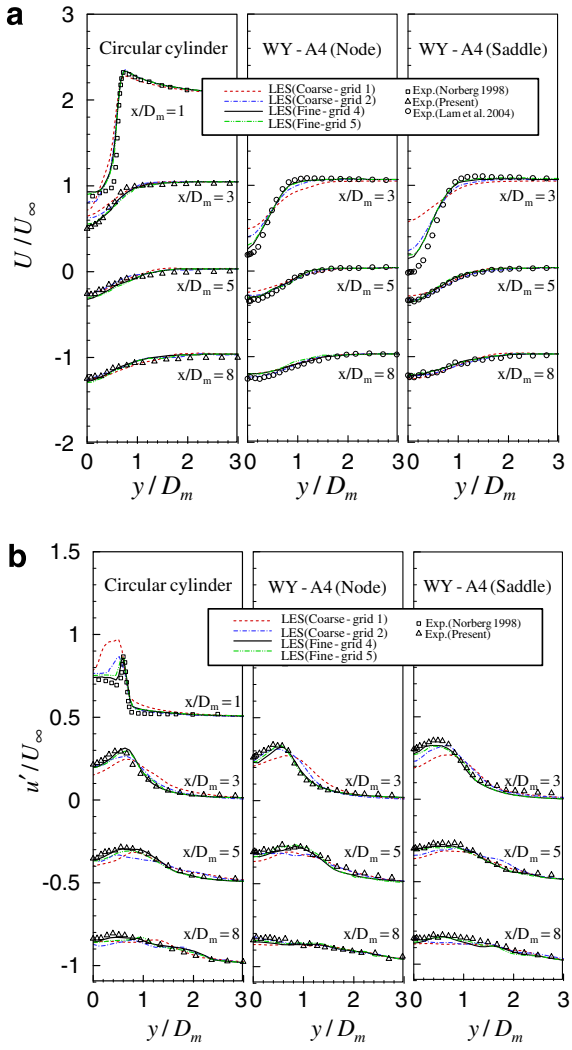

Fig. 3. Mean streamwise velocity U/U_∞ (a) and fluctuating streamwise velocity u'/U_∞ (b) distributions of a circular cylinder and a wavy cylinders (WY-A4) at different positions by LES method compared with experimental data at $Re = 3000$.

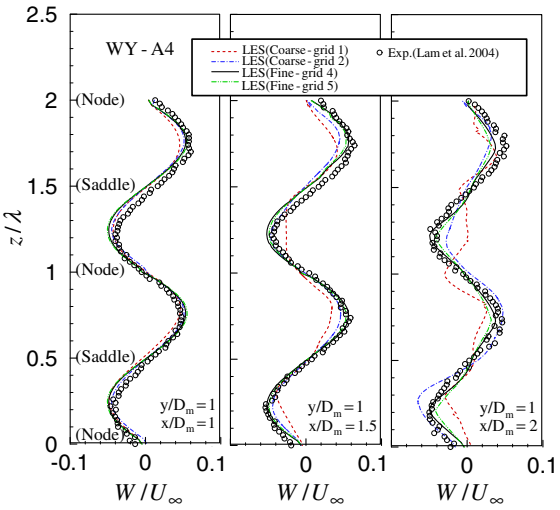

Fig. 4. Mean spanwise velocity W/U_∞ distributions of a wavy cylinders (WY-A4) by LES method compared with experimental data at $Re = 3000$.

tion of $x/D_m = 3$. That means, $x/D_m = 3$ is highly position sensitive region for the streamwise velocity distributions at such subcritical Reynolds number. A slight error in position may have a very different of the velocity profile. In general, it can be concluded that the results of the distributions of U/U_∞ and u'/U_∞ agree very well with that of the experimental results if the fine-grid models are employed.

Fig. 4 presents the nondimensional mean spanwise velocity W/U_∞ near the edge of the immediate near-wake ($y/D_m = 1$; $x/D_m = 1$, 1.5 and 2). Similar to the observations by Lam et al. (2004b), the spanwise velocity component of the wavy cylinder WY-A4 is zero at both the nodal and saddle plane. The significant spanwise flow goes from the saddle plane to the nodal plane. This kind of spanwise velocity distributions well illustrates that there is a high degree of three-dimensionality in the wake flow. Moreover, adopting the Fine-grid models 4 and 5, the LES results of W/U_∞ are very consistent with those LDA results by Lam et al. (2004b). All the comparisons above show that the present LES simulations can successfully predict the velocity distributions of the turbulent wake at different x/D_m and y/D_m values. Therefore, all these results gave us reasonable confidence on the application of LES model to capture and study the complex turbulent flow characteristics around wavy cylinders.

3.2. Force and Strouhal numbers of wavy cylinders

One of the major objectives of present investigation is to find an optimal range of wave geometries characterized by the different combinations of a/D_m and λ/D_m, which can well control the vortex structures of the wavy cylinders and hence reduce the mean drag and fluctuating lift. Fig. 5 shows that the mean drag coefficients $\bar{C}_D$ and fluctuating lift coefficients C'_L for different wavy cylinders models together with the mean values of a corresponding circular cylinder at $Re = 3000$. All the values of mean drag coefficients and fluctuating lift coefficients of the wavy cylinders are smaller than that of the circular cylinder. From the graphs in Fig. 5a and b, we can see that both corresponding values of the mean drag coefficients and fluctuating lift coefficients of wavy cylinders in group "WY-A" ($a/D_m = 0.091$) and in group "WY-B" ($a/D_m = 0.152$) are significantly reduced for the same value of nondimensional spanwise wavelength λ/D_m, especially for the wavy cylinders in group "WY-B". This is in consistent with the results obtained by Darekar and Sherwin (2001a). It can be concluded that by increasing in the amplitude of the wavy cylinder a/D_m, both the drag and lift fluctuation of wavy cylinder are reduced. Normally, a larger value of a/D_m will give a larger reduction of both the drag and suppression of the fluctuating lift.

Unlike the effect of a/D_m, the mean drag coefficient $\bar{C}_D$ of the wavy cylinders drops to a minimum at a certain

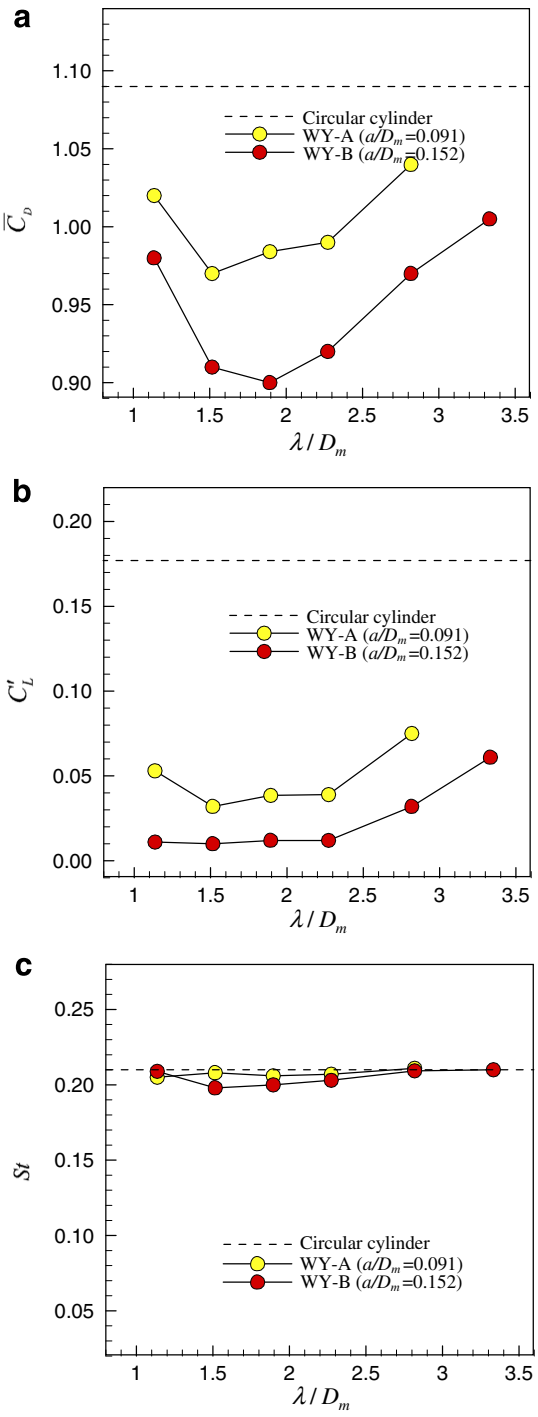

Fig. 5. Mean drag coefficients (a) and fluctuating lift coefficients (b) for wavy cylinders for different values of a/D_m and λ/D_m compared with a circular cylinder at $Re = 3000$; (c) Strouhal numbers of different wavy and circular cylinders at $Re = 3000$.

λ/D_m and increases again as λ/D_m increases. As shown in Fig. 5a, in the range of $\lambda/D_m = 1.136$–1.894, the mean drag force coefficients of the wavy cylinder are reduced quickly and the fluctuating lift force coefficients are also suppressed remarkably. Compared with a circular cylinder, the drag coefficient reduction up to 18% is obtained for the wavy cylinder model "WY-B3" ($a/D_m = 0.152$, $\lambda/D_m = 1.894$) at $Re = 3000$. For constant values of a/D_m, Lam et al. (2004a) found that with the value of $\lambda/D_m = 1.5$, a bigger reduction of drag can be obtained compared to that of $\lambda/D_m = 2.3$ for Reynolds numbers range from 20,000 to 50,000. It seems that a large value of wave steepness (a/λ) can further reduce drag. However, other experimental results by Nguyen and Jee (2004) showed that, with the values of $\lambda/D_m = 2$, wavy cylinders can get more drag reductions than that of $\lambda/D_m = 1$ at a wide range of Re from 5300 to 50,000. A maximum drag reduction up to 22% was obtained at $\lambda/D_m = 2$ and $Re = 10{,}000$. If the values of wave steepness (a/λ) are related with the drag reduction, the above two experimental results will be conflicting. The present LES results show that the above two experimental results are in fact not contradicting with each other. The disparity is due to the fact that the previous experimental investigations for the effect of λ/D_m were only performed in a small range and do not wholly reveal the effect of λ/D_m and a/D_m. With the present numerical simulation using the LES method to investigating flow around different wavy cylinders, it is relatively convenient to study a wide range of the combinations of λ/D_m and a/D_m, hence the significance of λ/D_m, a/D_m and a/λ can be better understood. Combined with the previous experimental data and our LES results, the optimal value of wavelength ratio for turbulent flow should be around $\lambda/D_m = 1.9$ with a large value of a/D_m. Regarding the fluctuating lift coefficient of the wavy cylinders, it can be seen that the values of C'_L in the wavy cylinder group "WY-B" ($a/D_m = 0.152$) are much smaller than others in the range of λ/D_m from 1.14 to 2.27. A maximum reduction of the fluctuating lift coefficient up to 94% is obtained at $a/D_m = 0.152$ and $\lambda/D_m = 1.515$. Although the value of $\lambda/D_m = 1.14$ is already not in the optimal range, the fluctuating lift coefficients are still significantly suppressed. As we have discussed above, the values of wave steepness (a/λ) are not directly related to the magnitude of drag reduction, but it may significantly control the vortex structures and hence suppress the fluctuating lift force (see Fig. 5b).

Fig. 5c shows that, the Strouhal numbers (St) of the wavy cylinders are all around 0.21, similar to that of the circular cylinder at the same Reynolds number of 3000. Only in the wavy model group "WY-B", the Strouhal numbers are slightly lower than that of the circular cylinders at the range of λ/D_m from 1.5 to 2. It can be concluded that the variation in surface geometry has little or no effect on the frequency of vortex shedding for the wavy cylinders. The Strouhal numbers of the three types of wavy cylinders measured by Lam et al. (2004a) also showed that the wave shape has little effect on vortex shedding of wavy cylinders at Re from 5000 to 60,000.

3.3. Vortex formation length and turbulence intensity

It is important to quantify the vortex formation length behind the cylinder because such length will affect the wake pressure and hence the force coefficient of the cylinder. The

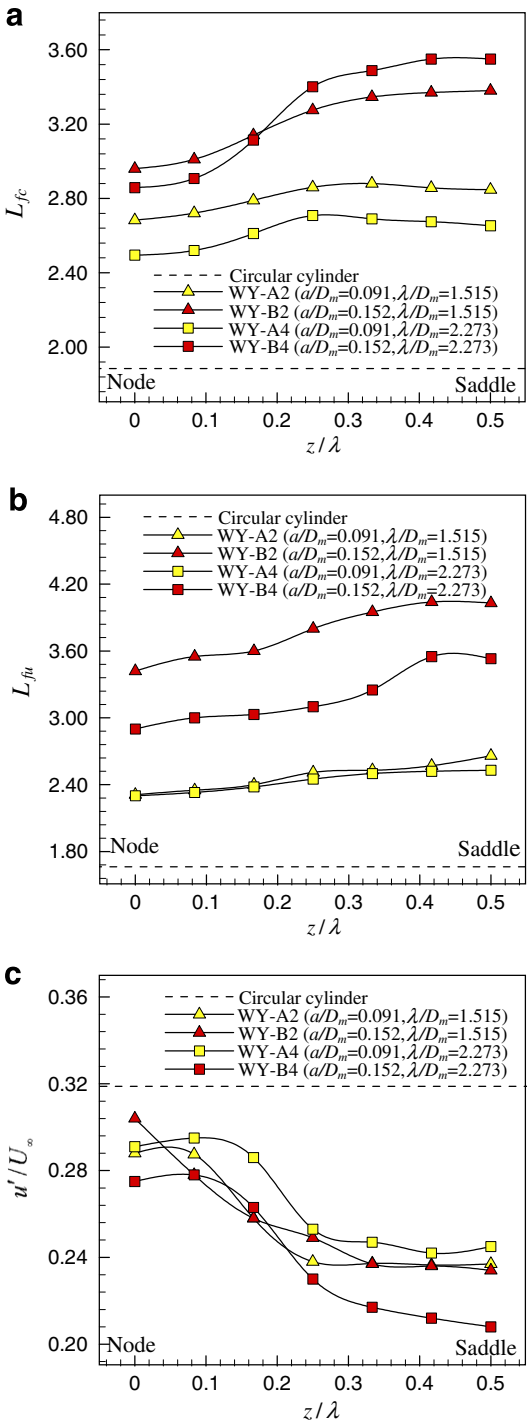

Fig. 6. (a) Vortex formation lengths (L_{fc}) for wavy and circular cylinders at $Re = 3000$; (b) the maximum turbulence intensity length (L_{fu}) and (c) the maximum values of turbulence intensity u'/U_∞ on the wake centerline of wavy cylinders compared with a circular cylinder at $Re = 3000$.

vortex formation lengths for various spanwise positions behind the wavy cylinders are shown in Fig. 6. The definitions of the length of vortex formation vary with different researchers. For example, Bloor (1966) defined the formation length as the point where low frequency irregularities suddenly decrease in intensity; Gerrard (1978) defined it as the point where the irrotational flow crossed the wake centerline behind the bodies and Norberg (1998) and Govardhan and Williamson (2001) defined the vortex formation length as the point on the wake centerline where the streamwise Reynolds normal stress reaches a maximum. Finally, the location of the time-averaged closure point on the wake centerline ($U/U_\infty = 0$) has been used to define the vortex formation length (Lam et al. (2004b)). In the present study, the normalized mean streamwise velocity U/U_∞ and normalized r.m.s. values of the fluctuating streamwise velocity (u'/U_∞) along the wake centerline ($y = 0$ plane) of the circular and wavy cylinders at the Reynolds number of 3000 are obtained. The wake closure length (L_{fc}) corresponding to $U/U_\infty = 0$ and the maximum turbulence intensity length (L_{fu}) where the turbulence intensity u'/U_∞ reaches a maximum along the wake centerline, are all calculated for different spanwise positions from node to saddle.

Fig. 6 shows the vortex formation lengths of four typical wavy cylinder models (WY-A2, WY-A4, WY-B2 and WY-B4) comparing with that of a circular cylinder at $Re = 3000$. Refer to Table 1, the wavy cylinder models WY-A2 and WY-B2 have the same wavelength ratio ($\lambda/D_m = 1.515$) but only distinguished by the value of a/D_m. Also, WY-A4 and WY-B4 have the same value of $\lambda/D_m = 2.273$. For all the cases of the wavy cylinders, the vortex formation lengths are evidently longer than that of the circular cylinder. Along the spanwise direction of wavy cylinders, the lengths of the vortex formation regions at the nodal planes are shorter than that of the saddle plane. The vortex formation length shows a large variation from the node to saddle for $a/D_m = 0.152$. In general, it increases from the nodal plane to saddle plane for all the wavy cylinders. Similar results were also found in experimental

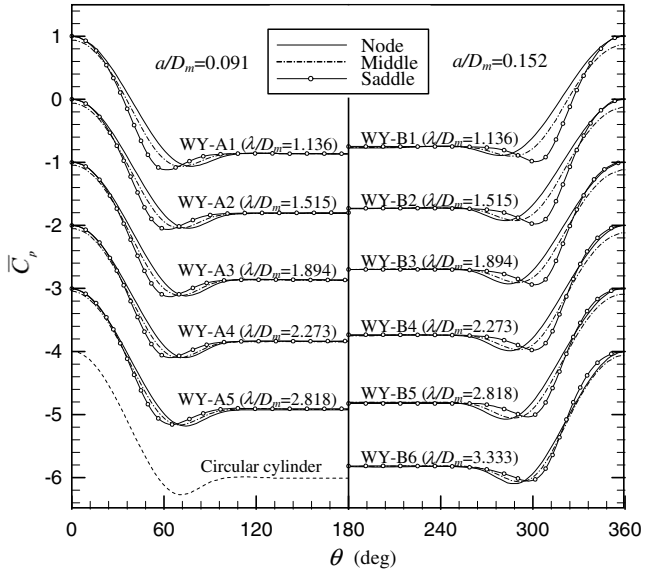

Fig. 7. Mean circumferential pressure coefficients distributions for wavy cylinders compared with that of a circular cylinder at $Re = 3000$.

measurements by Lam et al. (2004b) and Nguyen and Jee (2004).

Considering the base pressure of the different values of a/D_m and λ/D_m, shown in Fig. 7, the vortex formation lengths of wavy cylinders for group "WY-B" ($a/D_m = 0.152$) are longer than that for group "WY-A" ($a/D_m = 0.091$). Bearman (1965) showed that the vortex formation lengths of circular cylinders are inversely proportional to the mean base pressure coefficients $\bar{C}_{pb}$. Moreover we know that at the subcritical Reynolds number, the mean drag coefficient $\bar{C}_D$ is proportional to $-\bar{C}_{pb}$. So we can conclude that longer vortex formation regions

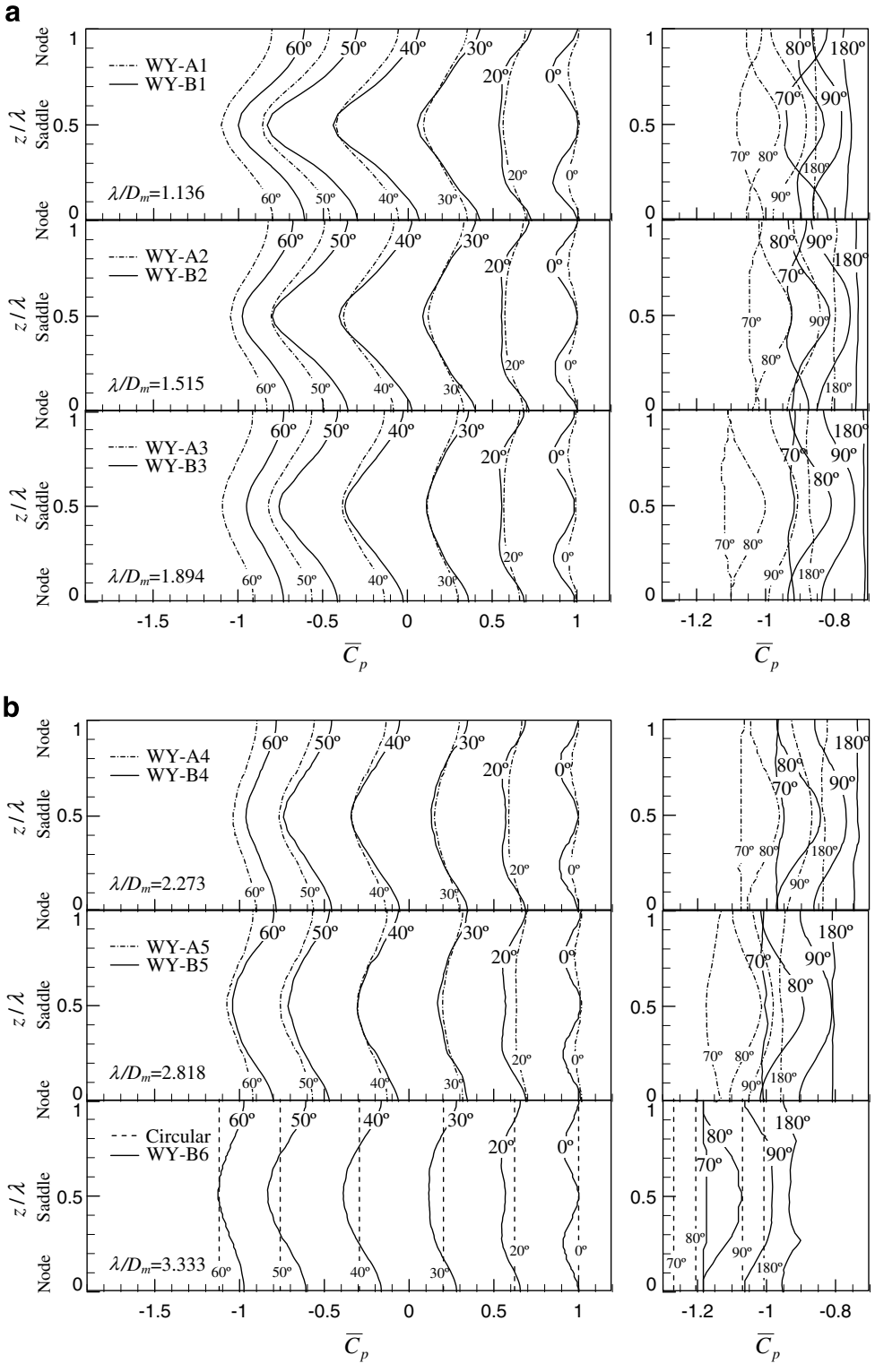

Fig. 8. Mean spanwise pressure coefficients distributions for wavy cylinders compared with that of a circular cylinder at $Re = 3000$.

can provide more reduction of the drag coefficient and an even greater suppression in the fluctuating lift coefficient. Also Bearman (1965) gave an expression for the formation length of circular cylinder $L_{fc}=C/(-\bar{C}_{pb})$. The value of C is in the range of 1.6–1.8 for the Reynolds range from 1000 to 9000. In present simulation, the formation length of circular cylinder using the Bearman (1965) expression is found to be have a value of $C=1.86$ at $Re=3000$, while, for the wavy cylinder, the value of C is in the range of 2.1–2.3 at $Re=3000$. Based on the results of the relationship between the drag force and the average formation length above, we obtained a maximum drag force reduction of 19% which is in good agreement with our simulation results of drag force reduction up to 18% as shown in Fig. 5a. So we concluded that the average vortex formation lengths of wavy cylinders are also inversely proportional to the mean drag coefficient $\bar{C}_D$ at the subcritical Reynolds numbers. Comparing the vortex formation length within the same group, it can be found that in group "WY-A" the formation lengths of WY-A2 are longer than WY-A4 in Fig. 6a. While the difference of formation lengths between WY B2 and WY B4 in group "WY B" is not very clearly distinguished. It seems that the effect of λ/D_m on the vortex formation lengths will be reduced with the increase of a/D_m.

Furthermore, the maximum turbulence intensity length (L_{fu}) where u'/U_∞ reaches a maximum along the wake centerline and the values of maximum u'/U_∞ along the wake centerline are also plotted in Fig. 6b and c. Comparing the values of L_{fu} in the same group, it can be found that in group "WY-A" the maximum turbulence intensity length changes only slightly with different values of λ/D_m, while the values of L_{fu} of WY-B2 are larger than that of WY-B4 as shown in Fig. 6b. So we can also infer that the effect of λ/D_m on L_{fu} will increase with the increase of a/D_m. Furthermore, as shown in Fig. 6c, a larger value of a/D_m will give rise to larger reduction of turbulence intensity u'/U_∞. From node to saddle, the maximum turbulence intensity length (L_{fu}) of wavy cylinders increases, while the value of u'/U_∞ decreases. In general, the values of turbulence intensity are all smaller than that of a circular cylinder. A longer turbulence intensity length and lower values of turbulence intensity would have obvious advantage on the minimization of fluctuating lift.

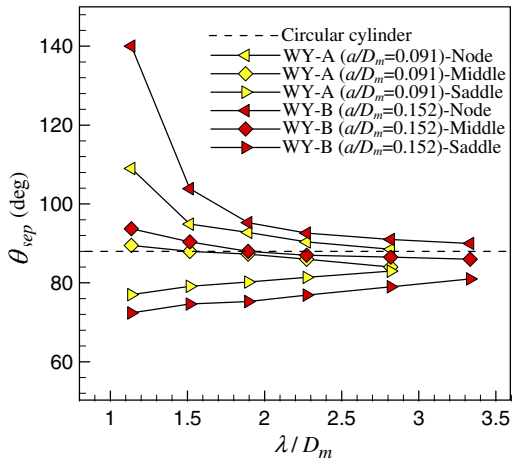

Fig. 9. Separation angles for wavy cylinders compared with that of a circular cylinder at $Re=3000$.

3.4. Pressure coefficients distributions

The drag reduction can also be understood by plotting the circumferential pressure distributions of wavy cylinders. The mean circumferential pressure coefficient $\bar{C}_p$ distributions of the wavy cylinders at different sections (node, middle, and saddle) are shown in Fig. 7. The corresponding circular cylinder at a Reynolds number of 3000 is also included for comparison. The lowest pressure coefficient points (the position of maximum negative pressure coefficients point) on the circular and wavy cylinders surface in present investigation are obtained. From Fig. 7, it can be seen that the lowest pressure coefficient point on the wavy cylinder varies in different cross sections. This means the separation at the saddle plane is much earlier than that

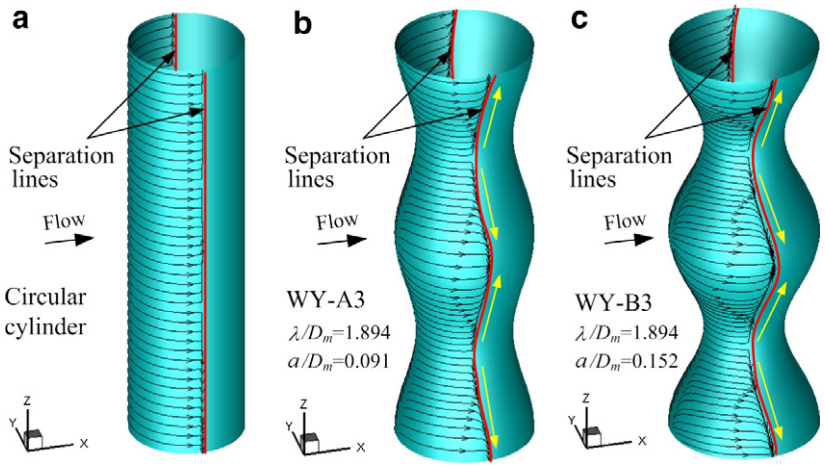

Fig. 10. Surface streamlines and the topology of the three-dimensional separation lines for the wavy and circular cylinders.

at the nodal plane for all wavy cylinders. It is also similar to the experimental results obtained by Ahmed and Bays-Muchmore (1992) and Lam et al. (2004a) In the range of smaller values of wavelength ($\lambda/D_m < 2$), the maximum negative pressure coefficients for the nodal planes are smaller than that at the middle and saddle planes. With the increase of λ/D_m, the difference of maximum negative pressure coefficients between node and saddle decreases. Especially for WY-B6 ($\lambda/D_m = 3.333$, $a/D_m = 0.152$), the maximum negative pressure coefficient at node is larger than that at a saddle which is very different with other models. But all the maximum negative pressure coefficients of the wavy cylinders in Fig. 7 are smaller than the corresponding circular cylinder. Also, we can observe that, with the increase of λ/D_m, the positions of lowest pressure coefficient points at different cross-sections are getting closer to the position of circular cylinders (71°) by the present LES method at $Re = 3000$. This also agrees with the value summarized by Norberg (2002). In wavy cylinder model group "WY-A" ($a/D_m = 0.091$), the lowest pressure positions seem closer to that of circular cylinders than in group "WY-B" ($a/D_m = 0.152$). That means a large value of a/D_m with a small value of λ/D_m can make a small value of lowest pressure position at a saddle plane and a large value of lowest pressure positions at a nodal plane. However, at the middle plane, the lowest pressure positions are still around the value of 71° (the position of lowest pressure coefficient points of a circular cylinder at $Re = 3000$). This kind of wavy variation of lowest pressure position for a wavy cylinder along the spanwise direction may lead to the flow separation line change from a straight line to a wavy line as well. Also the pressure distribution indicates that the pressure drop is more rapid and the separation is earlier at the saddle plane than those at other spanwise locations for wavy cylinders.

Furthermore, the variations of mean pressure coefficient along the spanwise direction at various angular locations ($\theta = 0°$, 20°, 30°, 40°, 50°, 60°, 70°, 80°, 90° and 180°) are shown in Fig. 8. It can be found that $\bar{C}_p$ at the stagnation points (0°) of nodal and saddle planes are about 1.0 for all wavy cylinders and are equal to that of the circular cylinder, while at other spanwise locations $\bar{C}_p$ is less than 1.0. The minimum values of $\bar{C}_p$ are located midway between the nodal and saddle planes of the wavy cylinders. Increasing the angular location, the minimum values of $\bar{C}_p$ are moved from the midway to the saddle plane (angular location > 20°) and the maximum values is still at the nodal planes. The maximum difference of $\bar{C}_p$ between nodal and saddle planes is found at $\theta = 40°$ for all the wavy cylinders. Further increasing the angular location, in the pressure recovery region behind the wavy cylinders ($\theta = 70$–180°), the minimum values of $\bar{C}_p$ change to the nodal planes while the maximum values are at saddle planes except the case of WY-B6 at $\theta = 180°$. All these characteristics are very different with that of the circular cylinder where $\bar{C}_p$ is constant along the spanwise direction. It may give rise to the three-dimensional effect for the near wake of the wavy cylinders.

From node to saddle, the variation pressure coefficients in the spanwise direction are more prominent in group "WY-B" than that in group "WY-A". That means a large value of wave amplitude a/D_m can lead to a large spanwise variation of the pressure distributions. Also shown in Fig. 8, the mean base pressure coefficients $\bar{C}_{pb}$ ($\theta = 180°$)

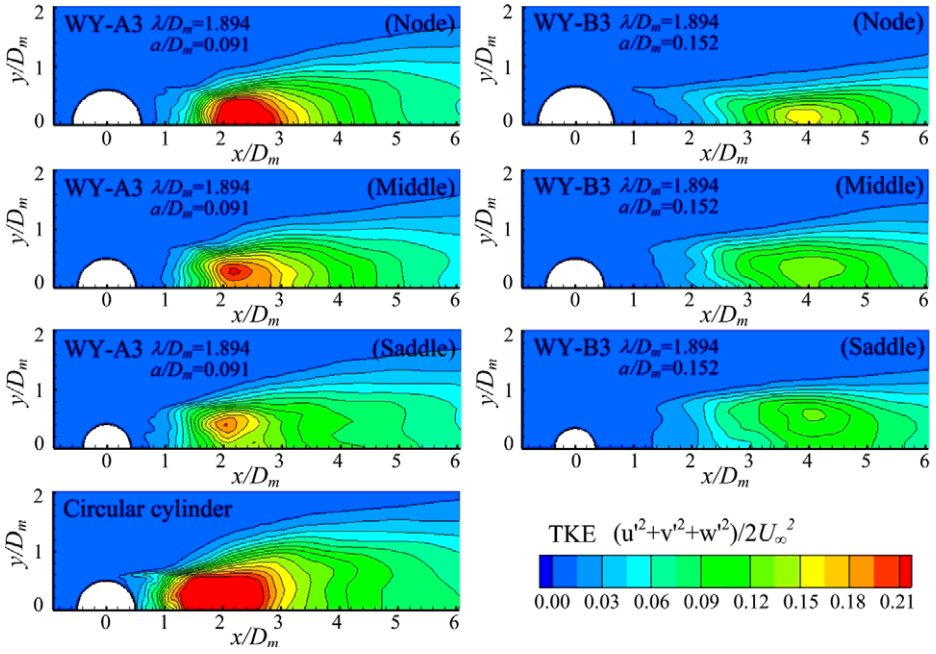

Fig. 11. Normalized x–y components turbulent kinetic energy (TKE) distributions at nodal, middle and saddle planes for wavy cylinders compared with that of a circular cylinder in the x–y plane.

of the wavy cylinders and the circular cylinder are obtained. And a larger value of a/D_m can lead to a larger value of base pressure coefficient which give rise to more drag force reduction. The mean base pressure coefficient $\bar{C}_{pb}$ changed from the nodal plane to the saddle plane and the $\bar{C}_{pb}$ value of nodal and saddle plane is slightly different especially for the models with large value of wavelength λ/D_m (WY-A4, WY-A5, WY-B4, WY-B5 and WY-B6). The base pressure coefficient distributes symmetrically with respect to saddle planes for smaller wavelength ($\lambda/D_m < 1.515$). Furthermore there are two peaks located symmetrically around the saddle plane of the model WY-B6 and the distance between these two peak is $0.55\lambda = 1.83D_m$ ($\lambda = 3.333D_m$). Also comparing with a circular cylinder, the $\bar{C}_{pb}$ values are all smaller and have important relationship with the vortex formation length and drag force as we discussed before.

3.5. Separation angles of wavy cylinders

The vortex shedding phenomenon is associated with flow separation from the boundary layer of bluff bodies. The flow separation points are referred to as the points on the surface of bluff bodies where the shear stress vanishes. Since the stability of the free shear layer and the resulting vortex structure are highly dependent on the separation point of the wavy cylinder, the flow separation angles (θ_{sep}) for both wavy and circular cylinders are obtained. As shown in Fig. 9, the flow separation angles in different cross sectional planes (nodal, middle and saddle) of wavy cylinders are plotted for $Re = 3000$.

With increase of the value of λ/D_m, the separation angles of the nodal plane reduce sharply at the range of λ/D_m from 1 to 1.5, while the reduction becomes smaller when the value of λ/D_m is larger than 1.5. At the nodal plane, the separation angle $\theta_{sep} = 140°$ for group "WY-B" ($a/D_m = 0.152$) is much larger than that of circular cylinders ($\theta_{sep} = 88°$). At the middle plane of wavy cylinders, the separation angles decreases slightly and still around the separation angle value of the circular cylinder at the same Reynolds number. At $\lambda/D_m < 2$, the value of separation angle is larger than that of circular cylinder while becomes smaller when $\lambda/D_m > 2$. Furthermore, at the saddle plane, the separation angle increases with the increase of λ/D_m. Here, all the values of separation angles are smaller than that of circular cylinders. Considering the effect of a/D_m, with a large value of a/D_m in group (WY-B, $a/D_m = 0.152$) the trance above becomes clear. That is to say, the wave steepness value a/λ plays an important role in separation point determination. Furthermore, there is some relationship between the separation angle and three-dimensional vortex structures. Lam et al. (2004b) pointed out the significant spanwise flow motion moving from the saddle plane toward the nodal plane, and depicted surface streamlines near the separation line similar to what is shown in Fig. 10 in the present simulation. Fig. 4 also confirmed this

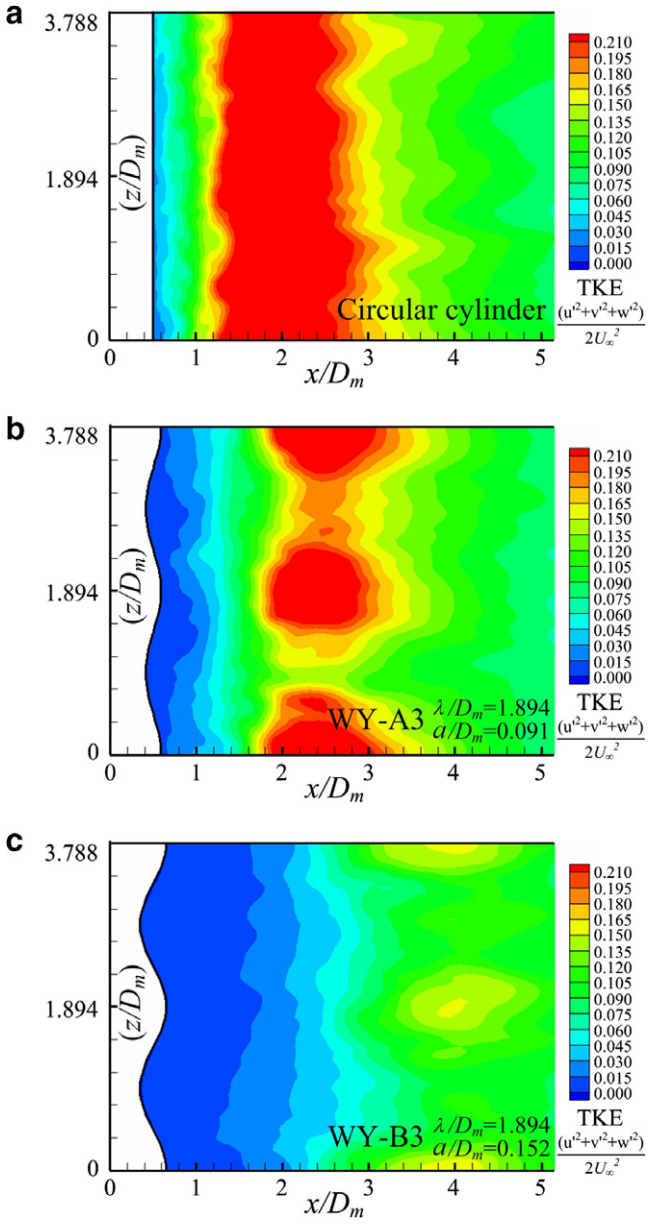

Fig. 12. Normalized x–z components turbulent kinetic energy (TKE) distributions at $y/D_m = 0$ for wavy and circular cylinders in the x–z plane.

kind of 3D flow characteristic. Moreover, a large value of wave steepness a/λ may enhance this 3D characteristic.

3.6. Turbulent kinetic energy

Fig. 11 shows the contour plots of the normalized turbulent kinetic energy (TKE) in the x–y planes [$\mathrm{TKE} = (u'^2 + v'^2 + w'^2)/2U_\infty^2$] of the wake behind the wavy cylinders [WY-A3 ($a/D_m = 0.091$, $\lambda/D_m = 1.894$) and WY-B3 ($a/D_m = 0.152$, $\lambda/D_m = 1.894$)] and a circular cylinder at $Re = 3000$. Both the TKE in nodal, middle and saddle planes are plotted for comparison. Compared with the circular cylinder, the region of negligible kinetic energy is noticeably larger behind the wavy cylinder than

that of a circular cylinder, especially for the wavy cylinder WY-B3 with a large value of a/D_m. The maximum TKE values and the high TKE values regime in the nodal plane are larger than that of the middle and saddle planes. These features are consistent with the elongation of the vortex formation length and the lower turbulence intensity mentioned above and shown in Fig. 6. However, all the TKE values for different cross-section planes of the wavy cylinders are smaller than that of the circular cylinder. Moreover, the positions of maximum TKE are farther away from the back of the wavy cylinder than that of the circular cylinder. Therefore, the overall TKE of the flow behind the wavy cylinder is lower than that of the circular cylinder at $Re = 3000$. It suggests that a wavy geometry can significantly reduce the TKE in the near wake.

In the x–z plane with $y/D_m = 0$, as shown in Fig. 12, the maximum TKE regime behind the circular cylinder is at around the position $x/D_m = 2$, and the values of TKE

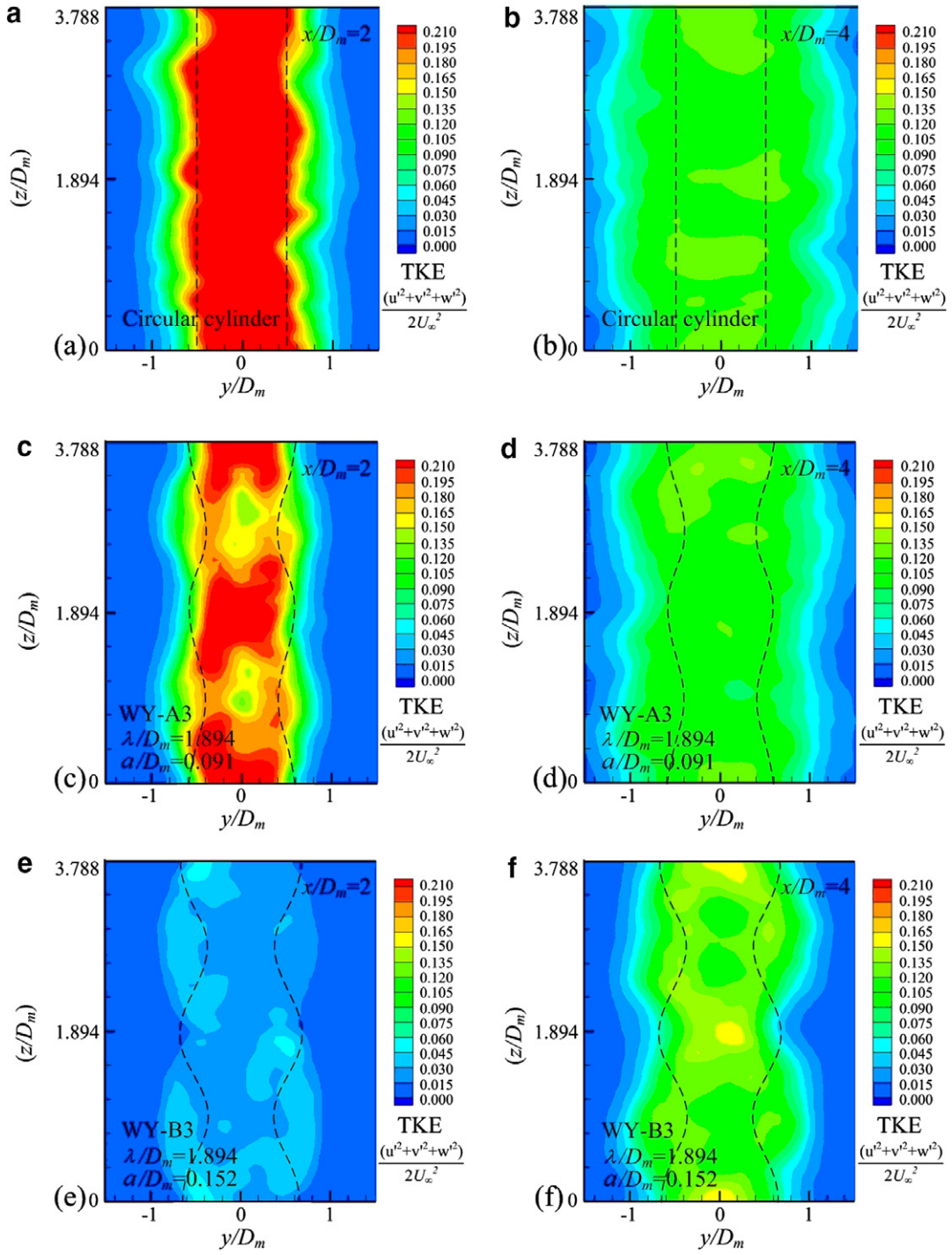

Fig. 13. Normalized y–z components turbulent kinetic energy distributions at $x/D_m = 2$ and 4 for wavy and circular cylinders in the y–z plane.

are uniform along the spanwise direction, while in the flow behind a wavy cylinder (WY-A3), at the downstream location of approximately $x/D_m = 2.5$, The TKE exhibits local maxima behind the nodes (see Fig. 12b). This is possibly due to the converging flow of the free shear layer from the saddle to the node (the significant spanwise flow goes from the saddle plane) and additional transport of kinetic energy near the node by the streamwise vortices. In the regimes behind the saddles of the wavy cylinder, the values of TKE are smaller than that behind the nodes, and lesser variation along the streamwise direction can be observed than those behind the nodes. In generally, the spanwise variation of TKE shows periodic repetition for wavy cylinders as contrast to the uniform distribution of the circular cylinder. Furthermore, the maximum values of TKE in spanwise direction for wavy cylinders are all smaller than that of the circular cylinder. The similar characteristics are found for the wavy cylinder (WY-B3) at the position $x/D_m = 4$ and weaker in strength (see Fig. 12c).

Fig. 13 shows the contours of the normalized TKE in the y–z plane at the downstream location $x/D_m = 2$ and 4 for the circular and wavy cylinders. For a circular cylinder, the TKE contours are nearly parallel to the cylinder axis. At the positions of $x/D_m = 2$, the significantly large value of TKE is in the wake center regime due to active momentum exchange, while decreases gradually along the crosswise direction. However, the TKE distributions of the flow behind wavy cylinders show periodic variations along the spanwise direction. Moreover, the TKE adjacent to the saddles are smaller than that at the nodes. Contrast with the circular cylinder, however, the values of TKE of the near-wake behind the wavy cylinders are smaller, especially at the saddles of the wavy cylinders. This indicates that for the wavy cylinder, the strength of TKE decreases substantially in the near-wake region which is the physical reason

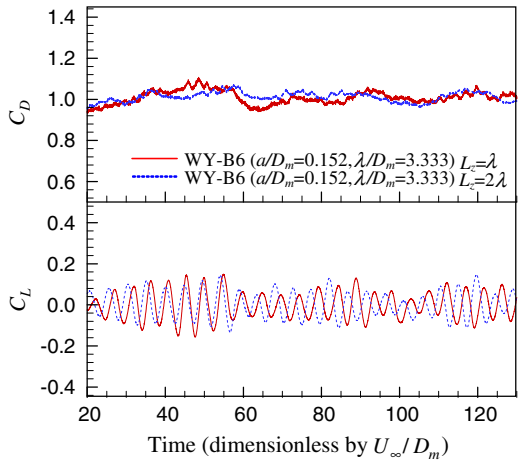

Fig. 15. Time history of drag and lift coefficients for the wavy cylinder (WY-B6) with different spanwise length in the computational domain.

for the reduction drag and fluctuating lift on the cylinder. In general, we can conclude that the flow around a wavy cylinder shows an evidently periodic characteristic in the flow pattern along the spanwise direction. This kind of wavy surface leads to a significant reduction of TKE and in turn, the reduction the drag and suppression of the fluctuating lift.

3.7. Three-dimensional vortex structures

The iso-surfaces of streamwise vorticity (ω_x) of the typical wavy cylinder (WY-B6) are shown in Fig. 14. The vortex structures of the wavy cylinder using a spanwise length $L_z = \lambda$ in the computational domain are plotted in Fig. 14a, contrasted to the cylinder with $L_z = 2\lambda$ in the computational domain in Fig. 14b. All the two figures exhibit

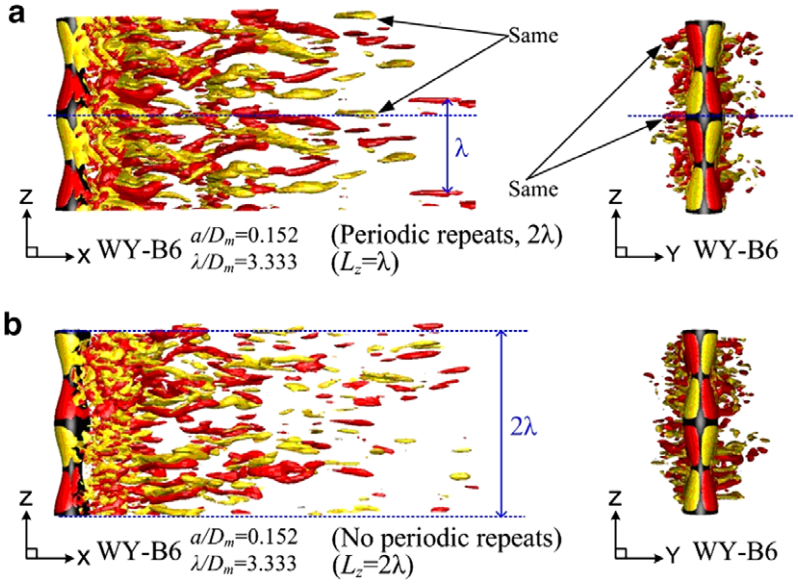

Fig. 14. Iso-surfaces of streamwise vortices ($\omega_x = \pm 1$) for the wavy cylinder (WY-B6).

similar periodic patterns along the spanwise direction with alternating negative and positive vortices and symmetrically distributed with respect to the central axis of the cylinders. Zhang et al. (2005) investigated a wavy cylinder with $\lambda/D_m = 2$ at the same Reynolds number using PIV method also observed this phenomenon. Moreover, the time history of drag and lift coefficients for these two wavy cylinder cases are also plotted in Fig. 15 which shows no distinction between the two cases. Considering the validation of the periodic boundary condition which we have discussed in Section 2, referring to Table 3, the consistent results here confirm that the periodic boundary condition with only one spanwise wavelength in the computational domain is also sufficient accurate to simulate flow pass a wavy cylinder.

Fig. 16 shows the iso-surfaces of crosswise vorticity patterns (ω_y) for several wavy cylinders at $Re = 3000$. With a small value of λ/D_m, the patterns of near-wake crosswise vorticity appear to be well organized and coherent. Increasing λ/D_m, this kind of vorticity pattern becomes chaotic. For example, the near-wake vorticity patterns of wavy models WY-A5 and WY-B5 ($\lambda/D_m = 2.818$) are similar to that of the circular cylinder. Furthermore, this periodic crosswise vorticity patterns are more coherent for larger values of wave amplitude $a/D_m = 1.515$ (group WY-B). That means a larger value of wave steepness a/λ can control and organize the vortex structures. As we discussed above, a/λ plays an important role in separation point determination. That is to say, the separation point has a strong relationship with the near wake vortex structures of the wavy cylinder. It was also confirmed by Zhang et al. (2005). Moreover, at the optimal range of wavelength (λ/D_m around 1.9), the iso-surfaces of crosswise vorticity behind the wavy cylinder shows distinctively regimes of zero vorticity (the recovery region) centered adjacent to the saddle planes. But no clear zero vorticity patterns can be found in other ranges of wavelength. The wave amplitude a/D_m affects the size of the zero vorticity regime. Large value of a/D_m can generate a large zero vorticity regime behind the wavy cylinder. While for the circular cylinder, no zero vorticity regimes can be observed. All the results above show that the wave steepness a/λ plays an

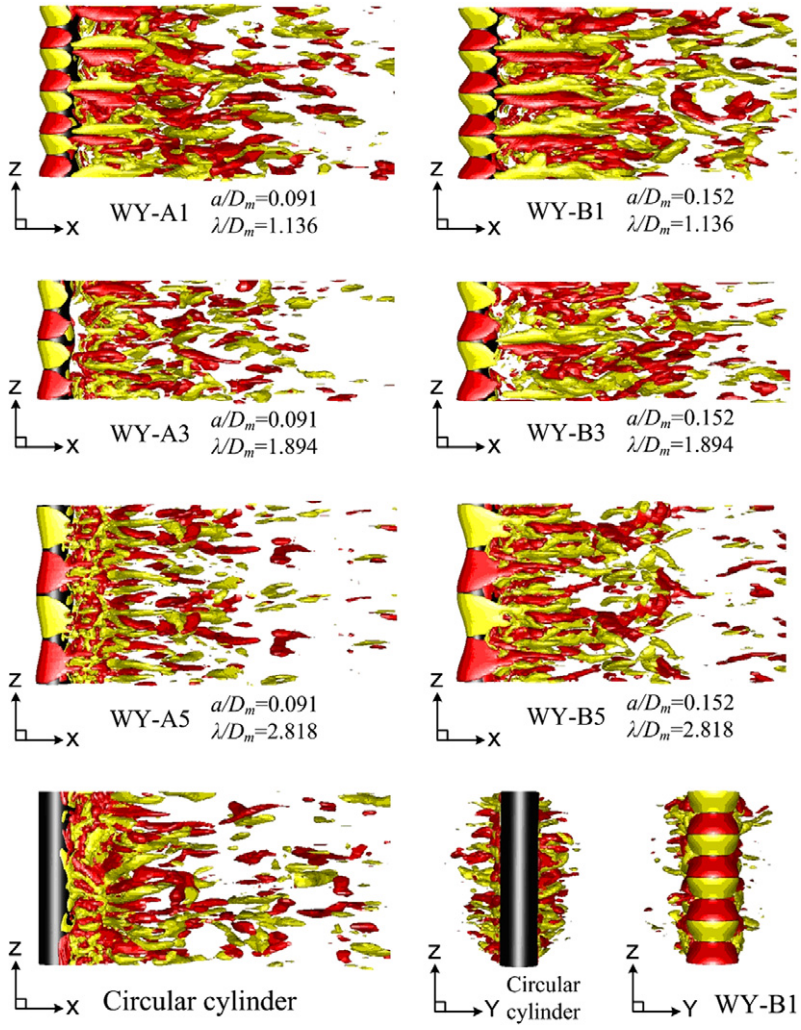

Fig. 16. Iso-surfaces of crosswise vortices ($\omega_y = \pm 1$) for wavy and circular cylinders.

important role in control and organizing the near wake vortex structures but no effect on the size of the zero vorticity regime behind the wavy cylinder. Refer to Fig. 5b, the wave steepness a/λ shows some relations with the reduction of fluctuating lift coefficient. A large value of a/λ may give rise to a small value of fluctuating lift coefficient by proper organizing the near wake vortex structures behind the wavy cylinders. It is interesting to find that the zero vorticity regimes of the wavy cylinders are only related to the wavelength λ/D_m. An optimal wavelength can generate a big size zero vorticity regime. That means the three-dimensional free shear layer generated from the wave surface is more difficult to roll up to vortex structure and it rolls up to mature vortex at a further downstream position in the cylinder wake. It also means a large value of vortex formation length which leads to the drag force reduction. Furthermore, the wave amplitude a/D_m always play a role in enhance the effect of vortex structures control, drag force reduction and the weakening the fluctuating forces which cause flow induced vibration (FIV).

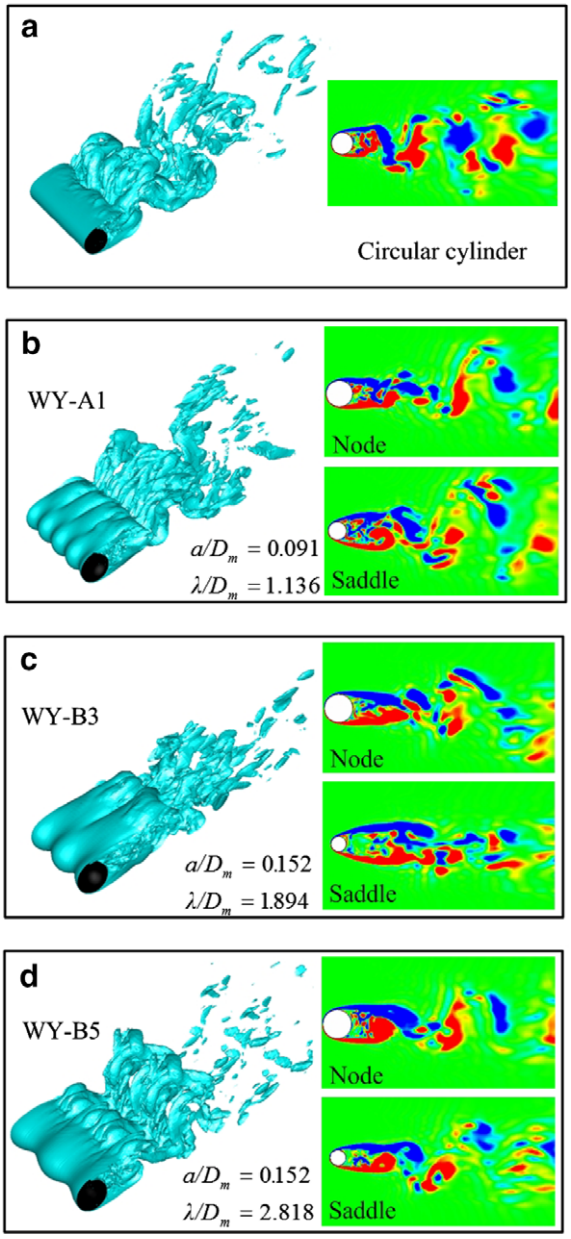

Fig. 17. Iso-surfaces of instantaneous vortices magnitude and the spanwise vorticity patterns in the flow over wavy cylinders compared with a circular cylinder.

The three-dimensional near wake vortex structure and the spanwise vorticity (ω_z) in nodal and saddle planes at optimal wavelength wavy cylinder (WY-B3) is shown in Fig. 17c compared with that of a circular cylinder. The structures for other wavy cylinders at the same Reynolds number are shown in Fig. 17a–d. The distinct difference in free shear layer development and vortex formation length are plotted. The spanwise vortex patterns at the nodal and saddle planes of the wavy cylinders are shed periodically and alternately with opposite rotation, which appear as negative vortices in the upper shear layer and positive vortices in the lower shear layer. Compared with a circular cylinder, the spanwise vortices contours in both the nodal and saddle planes of wavy cylinder are noticeably elongated towards the downstream direction, especially in group "WY-B" and with the optimal range of λ/D_m around 1.9. Due to the smaller separation angle at the position of saddle plane, the vortices expand along both the streamwise direction and the crosswise direction and the wake width at the saddle plane is increased giving rise to a wide wake at the further downstream. However, a large value of separation angle at the nodal plane suppresses the shear layer development. The vortices in the nodal plane seem to be extended only in the streamwise direction and noticeably suppressed in the crosswise direction. As a result, it produces a narrower wake downstream. Thus the flow structures of near wake have periodic variation along the spanwise direction of the wavy cylinders. Lam et al. (2004b) also showed the similar characteristic of a wavy cylinder at a wide range of *Re*. At both the nodal and saddle planes of the typical model WY-B3, the periodic vortex shedding can be found only at the further downstream position. This explains why the values of fluctuating lift coefficient are very small at the optimal range of wavelength λ/D_m around 1.9 in the group "WY-B". Because of these complex effects, the three-dimensional vortex sheet of wavy cylinders rolls up into a mature vortex further downstream from the cylinder as compared to the circular cylinder.

4. Conclusions

The turbulent flows past wavy cylinders are simulated using the large eddy simulation (LES) in the present study. The three-dimensional near wake vortex structures of wavy cylinders at *Re* of 3000 are obtained. Due to the wavy flow separation line along the spanwise direction of the wavy cylinders, the wake width expands in the region behind the saddles of cylinders and shrinks behind the nodes. As a result, the near wake vortex structures exhibits a periodic

variation along the spanwise direction. The Strouhal numbers for wavy cylinders are still approximately the same as that of a circular cylinder. That is to say, the vortex shedding of approximately similar frequency still occurred but the free shear layer is more difficult to roll up and develops to a mature vortex at a further downstream position by a longer vortex formation length. Hence, the effects of pressure and pressure fluctuation are less strongly felt by the cylinder. For such kind of wavy surface with certain critical values of λ/D_m and a/D_m, it can even significantly modify and control the three-dimensional vortex structures behind the wavy cylinder. As a result, it also weakens the vortex strength and increases the base pressure of the cylinder. The mean drag coefficient and the fluctuating lift force of wavy cylinders drop sharply with the increase of wave amplitude a/D_m at an optimal wavelength λ/D_m around 1.9. But it has little effect on the values of Strouhal numbers compared with a circular cylinder at the same Reynolds number. Furthermore, the vortices are well organized for a large value of wave steepness (a/λ) which has a strong effect on the fluctuating lift force. All the results above explained why some cylinders with certain spanwise waviness and wave amplitude could produce a significant drag reduction and suppression of the cylinders vibration.

Acknowledgements

The authors wish to thank the Research Grants Council of the Hong Kong Special Administrative Region, China, for its support through Grant No. PolyU 5311/04E.

References

Ahmed, A., Bays-Muchmore, B., 1992. Transverse flow over a wavy cylinder. Physics of Fluids A 4, 1959–1967.

Ahmed, A., Khan, M.J., Bays-Muchmore, B., 1993. Experimental investigation of a three-dimensional bluff-body wake. AIAA Journal 31, 559–563.

Bearman, P.W., 1965. Investigation of the flow behind a two-dimensional model with a blunt trailing edge and fitted with splitter plates. Journal of Fluid Mechanics 322, 215–241.

Bearman, P.W., Owen, J.C., 1998a. Reduction of bluff-body drag and suppression of vortex shedding by the introduction of wavy separation lines. Journal of Fluid and Structures 12, 123–130.

Bearman, P.W., Owen, J.C., 1998b. Suppressing vortex shedding from bluff bodies by the introduction of wavy separation lines. In: 1998 ASME Fluids Engineering Division Summer Meeting.

Bloor, S., 1966. The transition to turbulence in the wake of a circular cylinder. Journal of Fluid Mechanics 19, 290–304.

Breuer, M., 1998. Large eddy simulation of the subcritical flow past a circular cylinder: numerical and modeling aspects. International Journal of Numerical Method in Fluids 28, 1281–1302.

Dalton, C., Xu, Y., 2001. The suppression of lift on a circular cylinder due to vortex shedding at moderate Reynolds numbers. Journal of Fluids and Structures 15, 617–628.

Darekar, R.M., Sherwin, S.J., 2001a. Flow past a square-section cylinder with a wavy stagnation face. Journal of Fluid Mechanics 426, 263–295.

Darekar, R.M., Sherwin, S.J., 2001b. Flow past a bluff body with a wavy stagnation face. Journal of Fluids and Structures 15, 587–596.

Gerrard, J.H., 1978. Wakes of cylindrical bluff bodies at low Reynolds number. Philosophical Transactions of the Royal Society of London Series A – Mathematical, Physical and Engineering Sciences 288, 351–382.

Govardhan, R., Williamson, C.H.K., 2001. Mean and fluctuating velocity fields in the wake of a freely-vibrating cylinder. Journal of Fluids and Structures 15, 489–501.

Keser, H. Ibrahim, Unal, M. Fevzi, Bearman, P.W., 2001. Simulation of wake from a circular cylinder with spanwise sinusoidal waviness. In: Proceedings of the Second International Conference on Vortex Methods, Istanbul, Turkey, September 26–28, 2001, pp. 131–137.

Lam, K., Lin, Y.F., 2006. Numerical simulation on the control of drag force and vortex formation by different wavy (varicose) cylinders. In: Proceedings of the IUTAM Symposium on Flow Control and MEMS, vol. 1, 107 London, UK, 19–22 September.

Lam, K., Wang, F.H., Li, J.Y., So, R.M.C., 2004a. Experimental investigation of the mean and fluctuating forces of wavy (varicose) cylinders in a cross-flow. Journal of Fluids and Structures 19, 321–334.

Lam, K., Wang, F.H., So, R.M.C., 2004b. Three-dimensional nature of vortices in the near wake of a wavy cylinder. Journal of Fluids and Structures 19, 815–833.

Liang, C., Papadakis, G., 2007. Large eddy simulation of pulsating flow over a circular cylinder at subcritical Reynolds number. Computers & Fluids 36, 299–312.

Lilly, D.K., 1966. On the application of the eddy viscosity concept in the inertial subrange of turbulence. NCAR Manuscript, p. 123.

Lu, X., Dalton, C., Zhang, J., 1997. Application of large eddy simulation to flow past a circular cylinder. ASME Journal of Offshore Mechanics and Arctic Engineering 119, 219–225.

Nguyen, A.T., Jee, S.J., 2004. Experimental investigation on wake behind a sinusoidal cylinder. In: Proceedings of the Tenth Asian Congress of Fluid Mechanics, 17–21 May 2004, Peradeniya, Sri Lanka.

Norberg, C., 1987. Effects of Reynolds number and a low-intensity freestream turbulence on the flow around a circular cylinder, Publication 87/2, Department of Applied Thermodynamics and Fluid Mechanics, Chalmers University of Technology.

Norberg, C., 1998. LDV-measurements in the near wake of a circular cylinder. In: Proceedings of the 1998 ASME Fluids Engineering Division Summer Meeting, Washington, DC, FED-vol. 245, FEDSM98-5202.

Norberg, C., 2002. Pressure distributions around a circular cylinder in cross-flow. In: Proceedings of the Conference on Bluff Body Wakes and Vortex-Induced Vibrations, December, Port Gouglas, Australia, pp. 237–240.

Norberg, C., 2003. Fluctuating lift on a circular cylinder: review and new measurements. Journal of Fluids and Structures 17, 57–96.

Owen, J.C., Szewczyk, A.A., Bearman, P.W., 2000. Suppression of Kármán vortex shedding. Physics of Fluids 12, S9.

Smagorinsky, J., 1963. General circulation experiments with the primitive equations. I. The basic experiment. Monthly Weather Review 91, 99–164.

Sohankar, A., Davidson, L., Norberg, C., 2000. Large eddy simulation of flow past a square cylinder: comparison of different subgrid scale models. Journal of Fluids Engineering 122, 39–47.

Tomabzis, N., Bearman, P.W., 1997. A study of three-dimensional aspects of vortex shedding from a bluff body with a mild geometric disturbance. Journal of Fluid Mechanics 330, 85–112.

Williamson, C.H.K., Wu, J., Sheridan, J., 1995. Scaling of streamwise vortices in wakes. Physics of Fluids 7, 2307–2309.

Williamson, C.H.K., 1996. Vortex dynamics in the cylinder wake. Annual Review of Fluid Mechanics 28, 477–539.

Zhang, W., Dai, C., Lee, S.J., 2005. PIV measurements of the near-wake behind a sinusoidal cylinder. Experiments in Fluids 38, 824–832.